

Alma Mater Studiorum Università di Bologna
Archivio istituzionale della ricerca

Simultaneous measurements of liquid velocity and tracer concentration in a continuous flow stirred tank

This is the final peer-reviewed author's accepted manuscript (postprint) of the following publication:

Published Version:

Paglianti A., Montante G. (2020). Simultaneous measurements of liquid velocity and tracer concentration in a continuous flow stirred tank. CHEMICAL ENGINEERING SCIENCE, 216, 1-12
[10.1016/j.ces.2020.115495].

Availability:

This version is available at: <https://hdl.handle.net/11585/785473> since: 2020-12-24

Published:

DOI: <http://doi.org/10.1016/j.ces.2020.115495>

Terms of use:

Some rights reserved. The terms and conditions for the reuse of this version of the manuscript are specified in the publishing policy. For all terms of use and more information see the publisher's website.

This item was downloaded from IRIS Università di Bologna (<https://cris.unibo.it/>).
When citing, please refer to the published version.

(Article begins on next page)

Simultaneous measurements of liquid velocity and tracer concentration in a continuous flow stirred tank

A. Paglianti¹, G. Montante^{2,*}

¹ Dipartimento di Ingegneria Civile, Chimica, Ambientale e dei Materiali, Alma Mater Studiorum - Università di Bologna, via Terracini 34, 40131 Bologna, Italy

² Dipartimento di Chimica Industriale ‘Toso Montanari’, Alma Mater Studiorum - Università di Bologna, via Terracini 34, 40131 Bologna, Italy

Abstract

This work concerns the simultaneous measurements of the velocity of a liquid and of the concentration of a passive scalar in a standard geometry stirred tank provided with a continuous feed stream. The data are collected close to the tracer inlet on a vertical plane portion located in the vessel top region by a combined Particle Image Velocimetry and Planar Laser Induced Fluorescence system. The mean and fluctuating velocity and concentration components in the axial and radial directions obtained under stirred and unstirred conditions are presented. Following the definitions provided in the realm of the gradient diffusion hypothesis for the turbulent scalar transport, the measured variables are further exploited for the calculation of the turbulent viscosity, the turbulent diffusivity and their ratio, that is the turbulent Schmidt number. For the investigated conditions, the turbulent Schmidt number values are in the range 0.7-1.0, although significant local variations are observed.

Keywords: Mixing; passive scalar transport; Particle image velocimetry; Planar laser induced fluorescence; Gradient diffusion hypothesis; Turbulent Schmidt number.

*Corresponding Author (G. Montante)

1. Introduction

After the invention of the laser in the 1960s, the local flow characteristics of stirred tanks have been widely investigated by reliable and non-intrusive optical diagnostic techniques (Papadopoulos and Arik, 2004). As a result, a very wide experimental database is currently available for the description of the flow characteristics and the formulation of predictive models under a variety of geometrical and physical conditions, particularly in the case of batch reactors (Liu, 2012). By the application of Laser Doppler Anemometry (LDA) and, more recently, of Particle Image Velocimetry (PIV), detailed flow features, such as the trailing vortexes behind the Rushton Turbine blades (e.g. Yianneskis and Whitelaw, 1993; Doulgerakis et al., 2009), smallest scale variables, such as the turbulent dissipation rate (e.g. Escudie and Line, 2003; Baldi et al., 2004), two-phase flow characteristics, such as the effect of a dispersed phase on the liquid flow (e.g. Montante et al., 2012; Li et al., 2018), have been obtained. In addition, the development of Planar Laser Induced Fluorescence (PLIF) has allowed quantifying the evolution of scalar variables over space and time (Houcine et al., 1996), moving far from the uncertainties of visual estimation or pointwise methods and allowing the investigation of industrially relevant applications including for instance pharmaceutical systems (e.g. Stamatopoulos et al., 2016). The development and application of the above-mentioned experimental techniques have supported also the development of fully predictive modelling methods, that are required for the optimization of industrial mixing operations.

One relevant aspect related to the performances of stirred tanks concerns the time required to homogenize the concentration of passive scalars, that depends on the convective and diffusive transport of the scalar in the flowing liquid. The measurement of the fluid dynamics variables based on PIV in combination with that of the transport of scalar properties based on PLIF leads to a direct experimental determination of the transport process. Important contributions in this field have been already given in the investigation of different turbulent systems, such as confined liquid jets (Liu et al., 2006; Feng et al., 2007; 2010), cross flowing gas jets (Su and Mungal, 2004) and vortex reactors (Hitimana et al., 2019). Instead, to the best of our knowledge the simultaneous application of PIV and PLIF for the determination of fluid flow and scalar concentration variables in stirred tanks has never been performed.

Coupled with the liquid flow predictions, passive scalars transport in stirred tanks can be obtained by the solution of the convection-diffusion equation. In case of transitional or turbulent flow regimes, the fluid flow is typically obtained from Reynolds Averaged Navier-Stokes (RANS) equations or Large Eddy Simulation (LES) and the turbulent diffusion coefficient in the scalar transport equation is taken proportional to the turbulent viscosity, with the

proportionality constant defined as the inverse turbulent Schmidt number (Hartmann et al., 2006). In the realm of the Reynolds Averaged convection-diffusion equation, the gradient diffusion hypothesis for the turbulent scalar flux is the simplest (Combest et al., 2011) and the most widely adopted for stirred tanks (e.g. Coroneo et al., 2011) and stirred bioreactors (e.g. Delafosse et al., 2014). The dependency of the scalar transport predictions on the value of the turbulent Schmidt number is often considered a key issue in a wide range of applications, ranging from stirred tanks (e.g. Hariga et al., 2018) to environmental fluid mechanics (Gualtieri et al., 2017).

In the following, the details of the combined PIV/PLIF technique as applied to a continuous flow stirred tank are provided. The data are shown with the purpose to present a novel application of PIV and PLIF for the investigation of stirred vessels. A basis for the evaluations of closure terms in the scalar transport equations at the unresolved turbulent scales in stirred tanks is also obtained.

2. Materials and Methods

2.1 Experimental apparatus and fluids

The investigation concerned a standard geometry stirred tank made of Perspex, that is shown in Fig. 1a together with the PIV and PLIF instrumentation arrangement.

The cylindrical flat-bottomed tank had diameter $T=232$ mm and height $H=T$ and was equipped with four equally spaced vertical baffles of width $W=T/10$. It was closed with a flat lid provided with two 8.1 mm diameter holes for the feed streams entrance (F1 and F2) and one 20 mm diameter hole for the liquid outlet (F3), as schematically depicted in Fig. 1b. Agitation was provided by a standard Rushton turbine of diameter $D=T/3$ placed at the impeller off-bottom clearance $C=T/2$. The tank was placed inside a Perspex trough filled with demineralised water, in order to minimize refraction effects at the cylindrical surface of the vessel.

Before starting the continuous working mode, the stirred tank was filled with a demineralised water solution of Rhodamine-6G of concentration about equal to 0.04 mg/L, that matched the final fluorescent dye concentration at the complete homogenization, for quickly achieving steady-state conditions. Two reservoirs were adopted for the two inlet streams, which were fed to the stirred tank by two separate peristaltic pumps, while the outlet stream was stored in a single reservoir before disposal. The total feed flow rate was equal to 10.5 mL/s. It consisted of two streams: 5.1 mL/s of water solution of Rhodamine-6G of concentration equal to 0.08 mg/L and 5.4 mL/s of demineralized water, entering from F1 and F2 respectively. The experiments

were carried out without agitation and at the impeller speed $N=100$ rpm, that corresponds to the impeller tip speed $V_{tip}=0.41$ m/s and to the rotational Reynolds number $Re = 1.03 \times 10^4$.

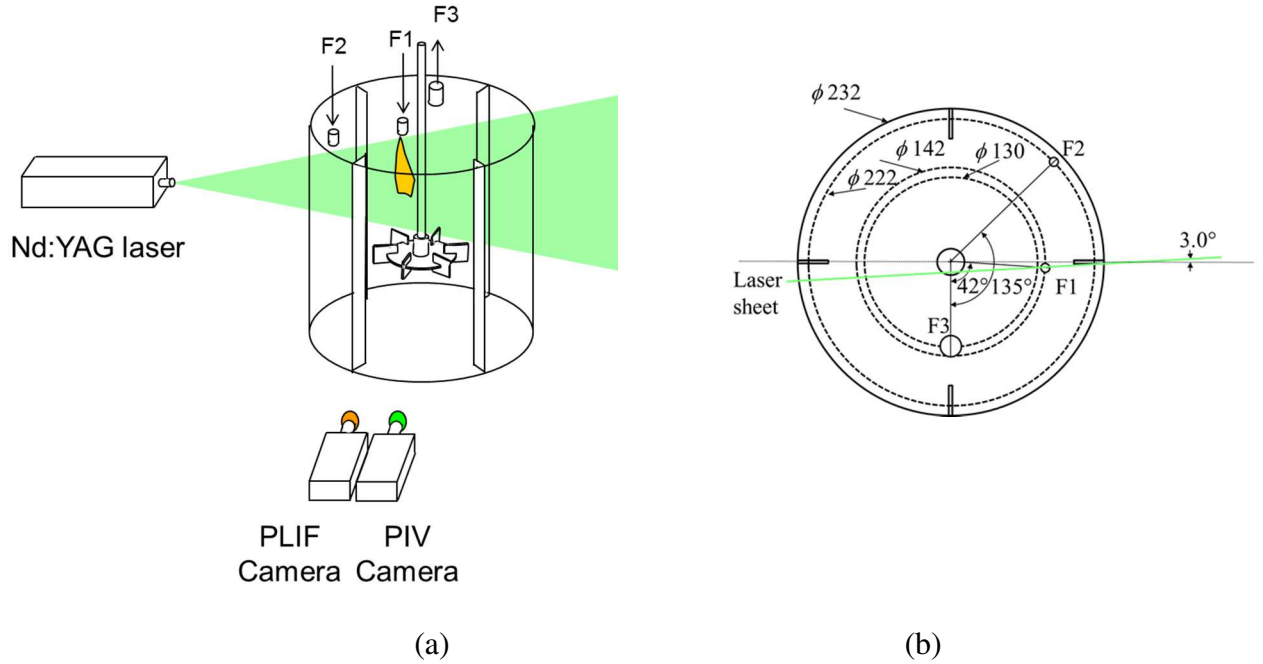


Fig. 1. Sketch of the experimental system. (a) PIV and PLIF measurements in the stirred tank; (b) top view of the vessel lid (dimensions in mm).

2.2 Measurement system

The simultaneous PIV and PLIF data were collected on a rectangular vertical section of $58 \text{ mm} \times 44 \text{ mm}$, located close to the inlet F1. The vertical laser light sheet, that entered the vessel in the position depicted in Fig. 1b, did not meet the shaft and the impeller, thus the disturbance due to the laser light reflections was reduced with respect to the case of diametrical plane illumination. Talc powder was adopted for seeding the liquid, for cheaply obtaining a good laser light scatter at the laser wavelength of 532 nm , while Rhodamine-6G was adopted as the passive tracer, since it emits the received laser light at 560 nm . The talc particle relaxation time based on the Sauter mean diameter of $13 \mu\text{m}$ and the density of 2820 kg/m^3 , is equal to $3.3 \times 10^{-12} \text{ s}$, that is very close to the value of classical liquid seeding particles (e.g. Poly Methyl methacrylate labelled with Rhodamine-B particles of mean diameter of $10 \mu\text{m}$ and density equal to 1190 kg/m^3). The talc particle size distribution was measured by a Malvern Spraytec instrumentation equipped with a Wet Dispersion Unit. By using two cameras provided with optical filters, each camera received the proper light signal. In particular the long-pass filter placed on the PLIF camera allowed to pass only waves whose length was longer than 550 nm to block the seeding particles scattered light, while the band-pass filter placed on the PIV

camera had central wavelength 532 nm and bandwidth ± 3 nm, to block the light emitted by the Rhodamine-6G.

The pulsed Nd:YAG laser ($\lambda=532$ nm, 15 Hz, 65 mJ,) and the two Charge-Coupled Device cameras (resolution of 1344×1024 pixels) were handled by a Dantec Dynamics “Timer Box” system. The time resolution of the synchronizer was equal to 12.5ns. Each camera was triggered with independent synchronization outputs.

The area viewed from the two cameras were identical, enabling an accurate overlap of the PIV and PLIF data. The thickness of the laser light sheet was equal to about 1.5 mm.

2.3 Analysis of PIV and PLIF raw images

The instantaneous velocity vectors were obtained from the cross-correlation of the PIV camera images collected in double-frame mode. The time interval between the two laser pulses was set to 800 μ s, the total number of image pairs, that ensured statistical convergence of mean velocities and turbulent fluctuations, was 2000, the acquisition frequency was equal to 6 images/s. A vector resolution of 0.3 mm was obtained by applying the cross-correlation on an interrogation area size of 16×16 pixels with an overlap of 50%. The instantaneous vectors were discarded if they did not fulfilled two conditions, one based on the evaluation of the peak heights in the correlation plane and the other on the velocity magnitude.

The instantaneous tracer concentration was obtained from the processing of the PLIF camera images collected in single frame mode with the exposure time of 1 ms. The raw instantaneous PLIF images were processed for eliminating the effect of the non-perfect uniformity of the laser light. To this end, the mean of 50 images collected with the initial seeded liquid only was subtracted to each instantaneous PLIF image. The image resulting from this operation was normalized by the difference between the mean value of 50 images collected at the dye concentration equal to 0.08mg/L and the mean of the 50 images collected initially. In this was the normalized concentration is equal to 0 before the tracer injection and goes to 1 when the tracer is homogenous on the plane. The concentration spatial resolution was equal to 0.09mm.

2.4 Constrains for the simultaneous application of PIV and PLIF

For the identification of the optimal measurement parameters and of the effect of the coupling of the two techniques on the accuracy of the results, additional preliminary tests were required with respect to the case of separate PIV and PLIF measurements, Particular attention was devoted to minimize the effect of the liquid seeding particles on the PLIF measurements and of the fluorescent dye on the PIV measurements. The seeding particle concentration of 6.0 mg/L was found to be the best compromise for having accurate PIV results, based on the number of

valid instantaneous velocity vectors after applying the selected validation criteria, and a negligible contribution of the laser light scattered by the seeding out the measurement plane on the PLIF measurements. The Rhodamine-6G concentration was selected considering that the maximum dye concentration for obtaining a linear relationship between local intensity of fluoresced light and local dye concentration was equal to 0.08 mg/L. At this concentration a negligible error in the tracer concentration estimation due to the light attenuation of the measured signal along the radial coordinate was detected. The absorption of Rhodamine-6G on the talc particles was negligible considering that each measurement lasted less than 6 minutes and for contact time of 30 minute it was found to decrease the emitted light intensity of 4%. Also, the shot-to-shot laser power variations was monitored and the signal was found suitable for the PLIF measurements, as in previous investigations (e.g. Coroneo et al., 2011; Busciglio et al., 2015).

2.5 Post-processing of the measured velocity and concentration data

In the following, the origin of the cylindrical coordinate system is placed on the centre of the tank bottom. The radial coordinate, r , is positive if directed toward the vessel wall, the axial coordinate, z , is positive if directed upwards. It is worth observing that since the laser light sheet entered the vessel vertically with an angle of 3° with respect to the radial direction, the radial velocity component is overestimated of 0.13%. Following the classical nomenclature adopted in the fluid mixing field, U and V are the mean axial and radial velocity components, u' and v' are the axial and radial root mean square (rms) velocity fluctuations. In addition, Φ is the mean tracer concentration and ϕ' is the rms concentration fluctuation. The variations of velocity and concentration along the tangential coordinate, θ , were not measured.

The normal and shear stress components $-\rho\overline{u'^2}$, $-\rho\overline{v'^2}$, $-\rho\overline{u'v'}$ and the axial and radial fluxes $\rho\overline{u'\phi'}$, $\rho\overline{v'\phi'}$ were measured with and without agitation.

Based on the map of the Kolmogorov length scale, λ , shown in Fig. 2, the spatial resolution of the PIV measurement was within the limit of 5λ (Liu et al., 2006).

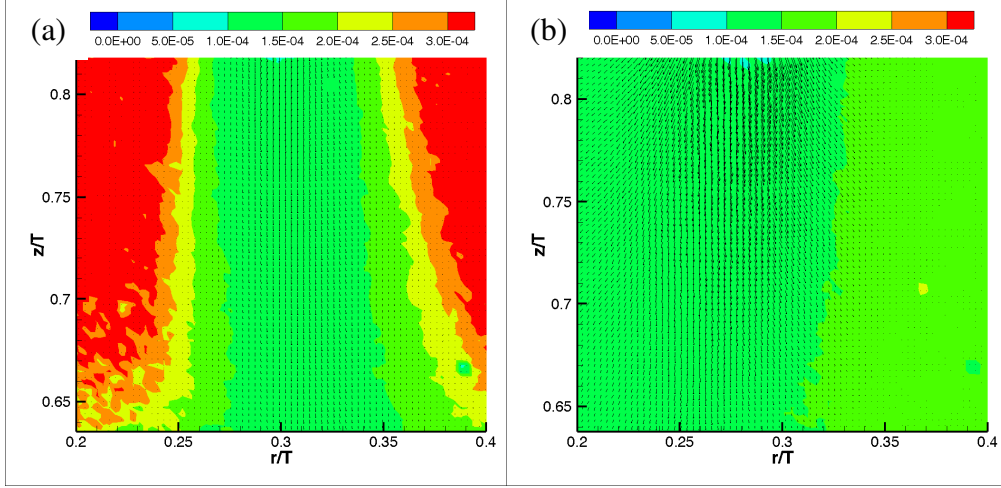


Fig. 2. Map of estimated λ . (a) $N=0$ rpm; (b) $N=100$ rpm, (colour scale in m).

The maps of λ were determined using the approximate value of the turbulent dissipation rate (Baldi and Yianneskis, 2003), ε , as:

$$\varepsilon = A \frac{u'^3}{\Lambda} \quad (1)$$

where A is a constant taken equal to 1, Λ is the integral length scale taken equal to the inlet stream width and u' is a characteristic fluctuating velocity (Feng et al., 2005), whose local value was obtained by the PIV measurements. It is worth observing that in the map shown in Fig. 2b λ is in the range of 0.1 - 0.2 mm, similarly the average value calculated from the overall dissipation rate based on the impeller power number is about equal to 0.1 mm. The values obtained just in the inlet stream region in the case of unstirred conditions shown in Fig. 2a have the same order of magnitude.

The spatial resolution of the PLIF measurements was about twenties the Batchelor scale, λ_B , defined as:

$$\lambda_B = \frac{\lambda}{\sqrt{Sc}} \quad (2)$$

where Sc is the Schmidt number of the Rodhamine-6G in water, that is equal to 1250 (Feng et al., 2010).

Due to the different resolution of the PIV and the PLIF data, for the turbulent fluxes calculations, the concentration data were resampled on a coarser grid coincident to that adopted

for the velocity vectors. The same grid was used for the calculation of the gradients of the mean velocity and mean concentration, that were based on second-order central differences. The mean and the turbulent fluctuations of the water velocity and the Rodhamine-6G concentration with and without agitation are examined and compared close to inlet region. The velocities are made dimensionless with the inlet stream superficial velocity and the concentrations are made dimensionless using the raw PLIF data processing method described in Section 2.3.

3. Results and Discussion

3.1 Liquid velocity field and Reynolds stresses

The mean axial velocity maps shown in Fig. 3 provide a clear indication of the interaction between the impeller stream and the inlet stream that was already widely discussed by Busciglio et al. (2015) and that is confirmed also under the operating conditions selected for this investigation, that are slightly different.

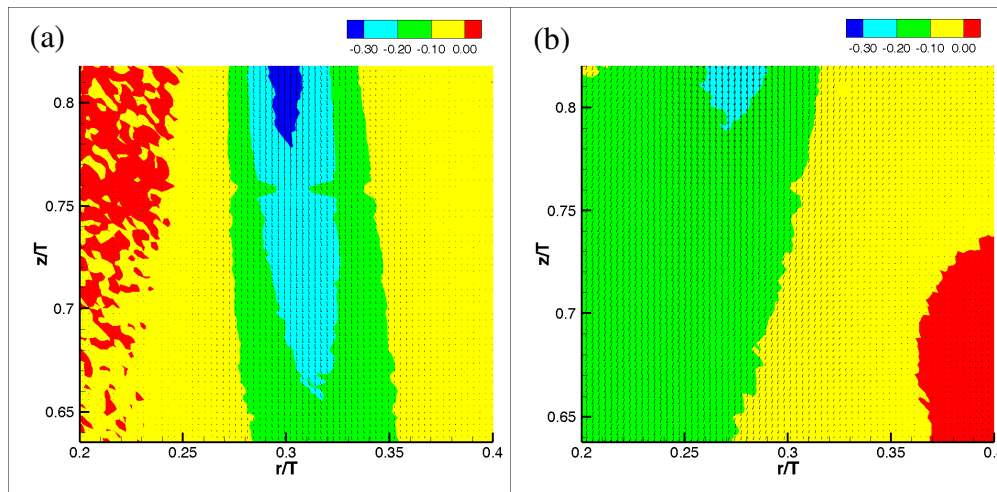


Fig. 3. Colour map of normalized U . (a) $N=0$ rpm; (b) $N=100$ rpm.

Similarly, the Reynolds stresses shown in Fig. 4 are visibly affected by the impeller action.

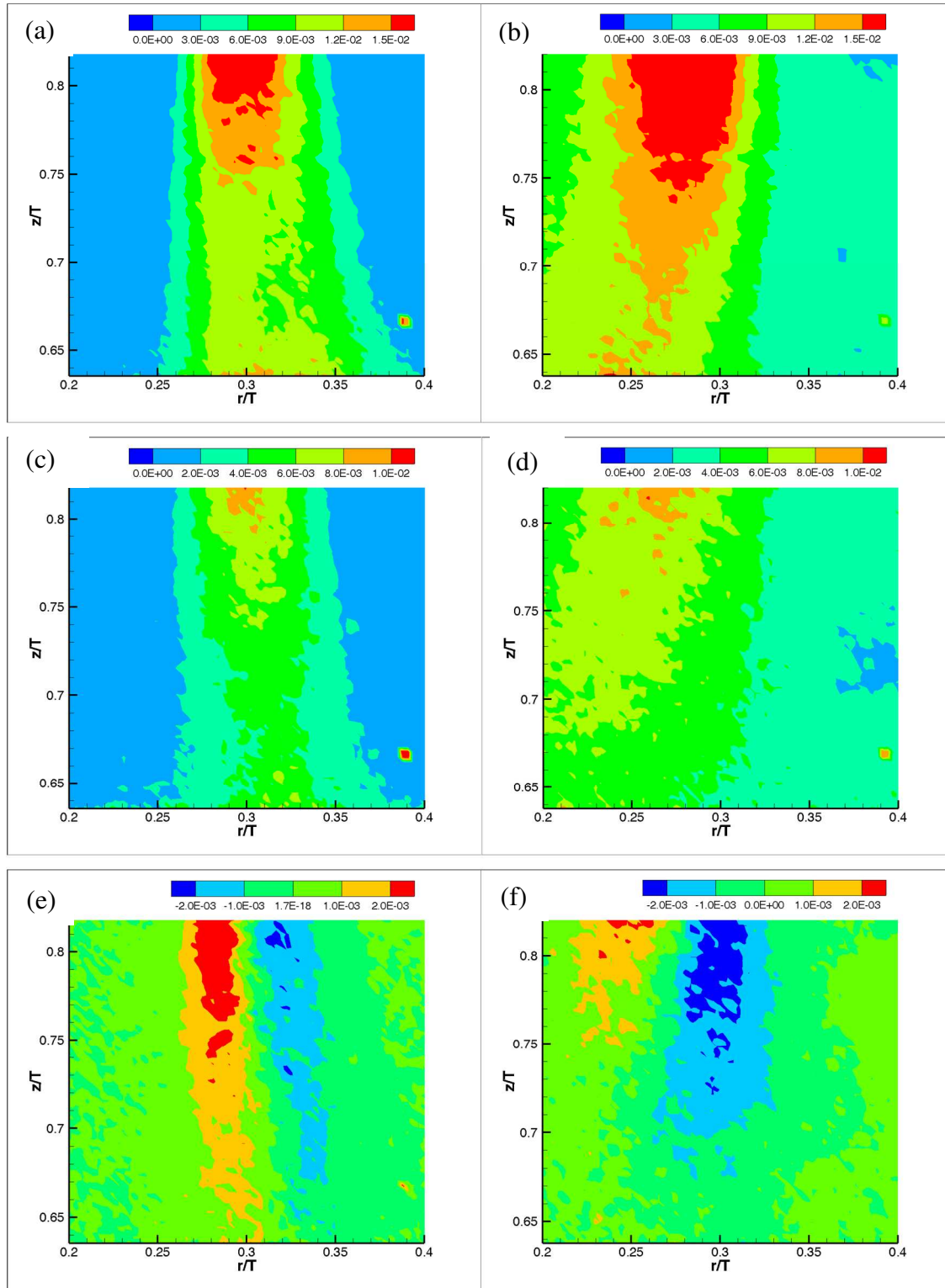


Fig. 4. Colour map of the normalized Reynolds stress tensor components. (a), (b): axial normal stress; (c), (d) radial normal stress; (e), (f) shear stress. (a), (c), (e): $N=0$ rpm; (b), (d), (f): $N=100$ rpm.

Whether with or without agitation, the axial normal stress magnitude is about double than the radial normal stress. Also, the shear stress changes sign at the inlet stream centreline in both the cases, since the radial velocity fluctuations are negative where the mean radial velocity is positive and vice versa.

3.2 Tracer concentration and turbulent fluxes

The mean tracer concentration shown in Fig. 5 clearly indicates very poor axial mixing when the inlet streams enter the unstirred fluid, while it exhibits a significant reduction in the axial direction when the inlet stream enters the stirred vessel. In the radial direction, a marked concentration reduction moving far from the axis of the jet is detected also with the stopped impeller.

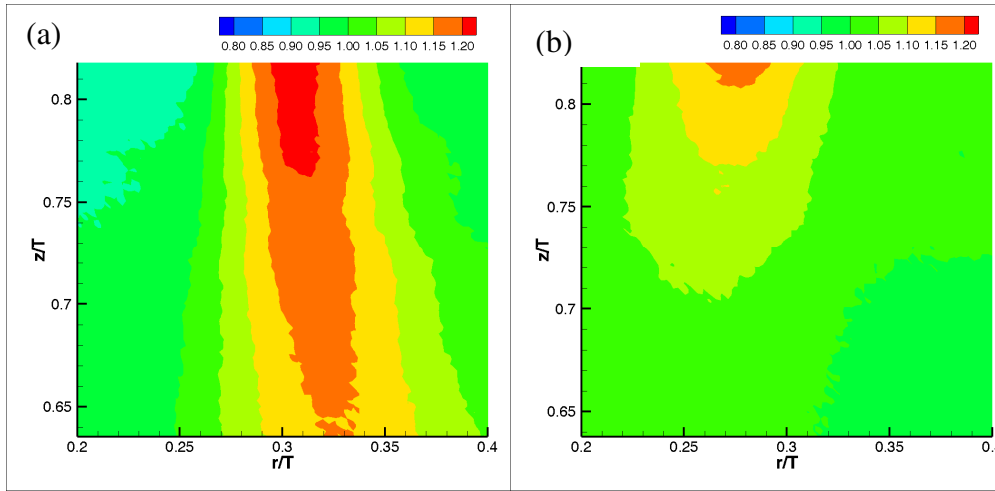


Fig. 5. Colour map of normalized Φ . (a) $N=0$ rpm; (b) $N=100$ rpm.

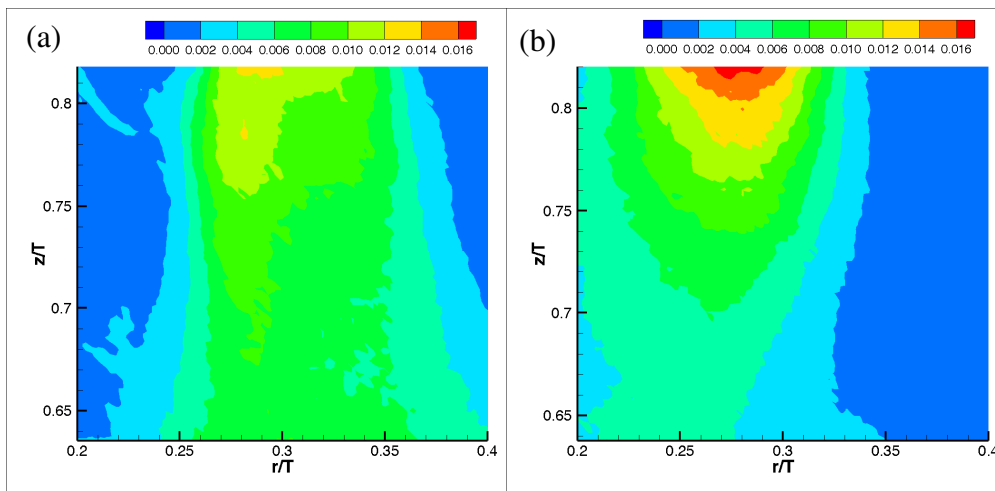


Fig. 6. Colour map of normalized ϕ' . (a) $N=0$ rpm; (b) $N=100$ rpm.

The fluctuations of the tracer concentration, that are shown in Fig. 6, are definitely affected by agitation, that makes the gradient of the fluctuations along the radial and the axial direction qualitatively similar to the mean values of the concentration.

The two components of the turbulent fluxes obtained by the combined PIV and PLIF measurements relevant to the inlet stream entering in the unstirred fluid and to the inlet stream interacting with the impeller stream are the shown in Fig. 7.

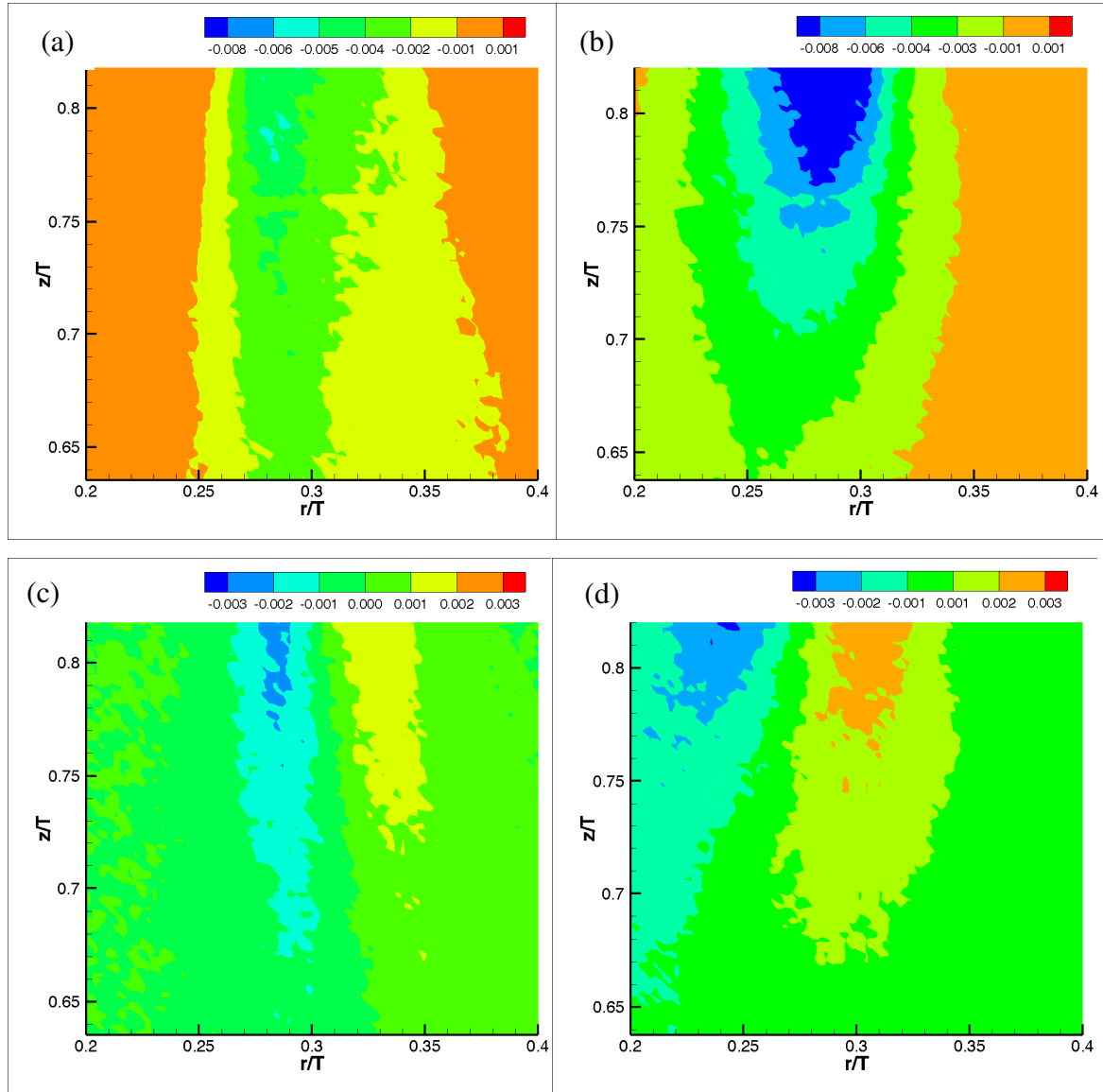


Fig. 7. Colour map of the normalized turbulent flux. (a), (b): axial turbulent flux; (c), (d) radial turbulent flux. (a), (c): $N=0$ rpm; (b), (d) $N=100$ rpm.

In both conditions, the radial and the axial components of the Reynolds flux are significantly different. The axial flux is symmetric with respect to the inlet stream axis and is much bigger

in magnitude than in the radial direction, similarly to the Reynolds stresses that exhibited higher values in the axial than in the radial direction. The radial flux is negative on the left of the inlet stream centreline and is positive on the right, that is opposite to the Reynolds shear stress and the mean concentration gradient shown in Fig. 5.

In order to observe the overall Reynolds flux on the plane, in Fig. 8, the vectors representing the Reynolds flux and the colour maps representing the angle formed by the vectors with the vertical direction, that is positive moving clockwise, are shown. As can be observed, in the inlet stream region of the stirred tank the passive scalar is transported from the turbulent flow in opposite directions with respect to the jet centreline. Close to the inlet centreline the action of the turbulent transport is similar with and without agitation, while the spatial extension of the turbulent transport action is much wider in the case of stirred fluid, as expected.

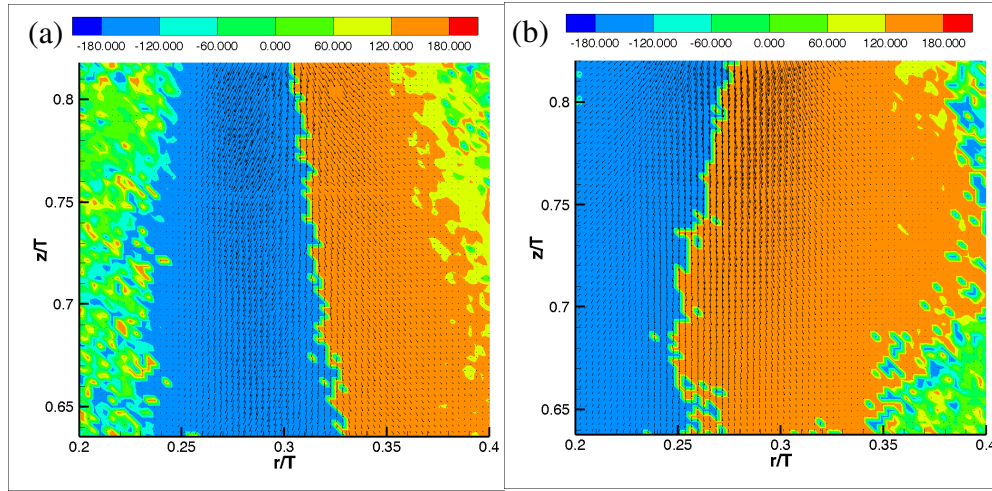


Fig. 8. Map of the turbulent flux angle superimposed to the vector plot of the dimensionless turbulent flux. (a) $N=0$ rpm; (b) $N=100$ rpm. Colour scale [degree].

3.3 Turbulent viscosity, turbulent diffusivity and turbulent Schmidt number

For application of the Reynolds averaged momentum and scalar transport equations, that are widely adopted in the Computational Fluid Dynamics simulations of stirred tanks, generally simple closure models for both the Reynolds stress tensor and the Reynolds flux are adopted. As for the former, the capabilities and the limitations of a wide variety of single-phase turbulence models have been evaluated, while for the latter the gradient diffusion hypothesis is mostly adopted for stirred tanks. For this reason, from the experimental data the kinematic turbulent viscosity, μ_t/ρ , the turbulent diffusivity, Γ_{22} , and their ratio, that is the turbulent Schmidt number Sc_t , are calculated using the following equations based on the well-known Boussinesq hypothesis and gradient diffusion models, respectively:

$$\nu_t = \frac{-\overline{u'v'}}{\partial U/\partial r + \partial V/\partial z} \quad (3)$$

$$\Gamma_{22} = \frac{-\overline{v'\phi'}}{\partial \phi/\partial r} \quad (4)$$

In addition the Γ_{12} , component of the turbulent diffusivity tensor was estimated, as:

$$\Gamma_{12} = \frac{-\overline{u'\phi'}}{\partial \phi/\partial r} \quad (5)$$

The turbulent viscosity is defined as the ratio of the Reynolds stress tensor and the mean velocity gradient. Of the different possible Reynolds stress components and mean velocity gradients, the definition provided by Eq. (3) is considered, since in the measurement region the main mean velocity component is in the axial direction and the gradient of the axial velocity in the radial direction is the prevailing one. These features can be clearly appreciated from the colour map of the mean velocity derivatives reported in Fig. 9 and Fig. 10, for unstirred and stirred conditions, respectively. The same colour scale is selected for all the derivatives for better appreciating the relative importance of the different terms.

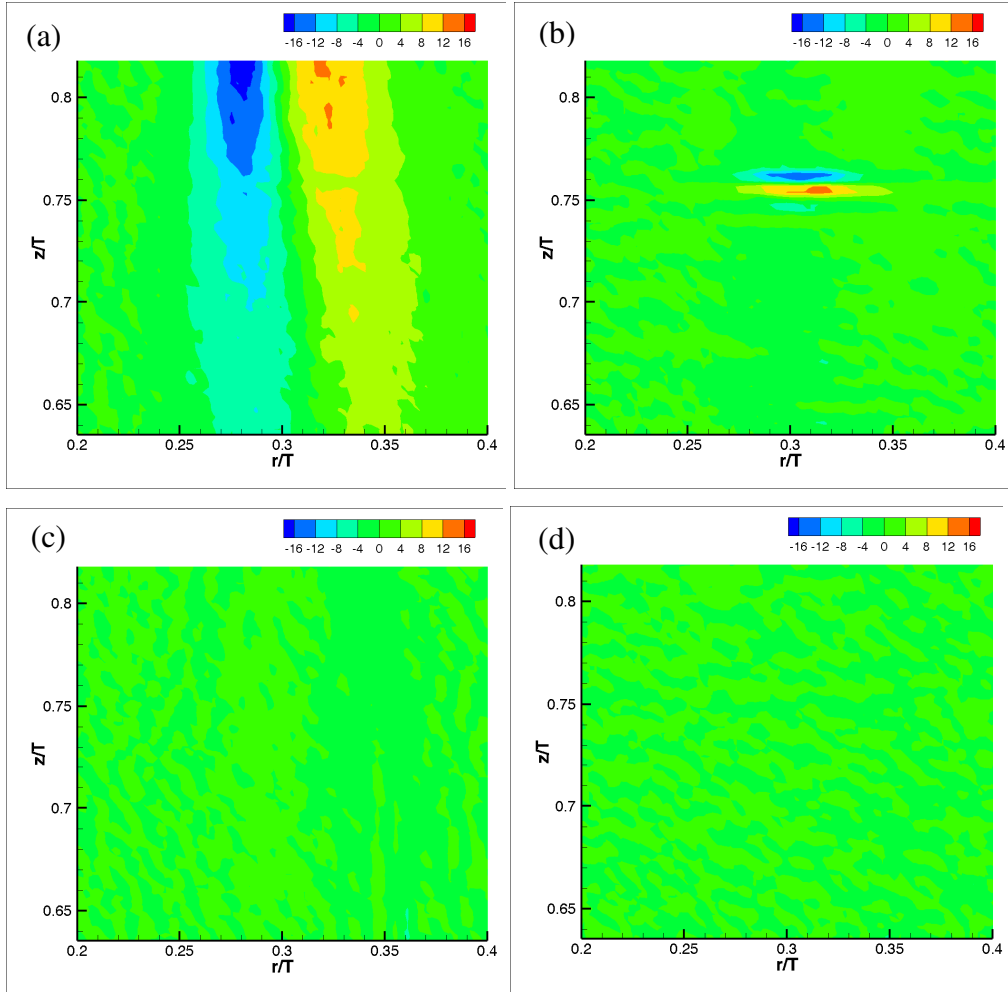


Fig. 9. Colour map of the derivative of the velocity. (a) $\frac{\partial U}{\partial r}$, (b) $\frac{\partial U}{\partial z}$; (c) $\frac{\partial V}{\partial r}$; (d) $\frac{\partial V}{\partial z}$, $N=0$ rpm.

Colour scale [s^{-1}].

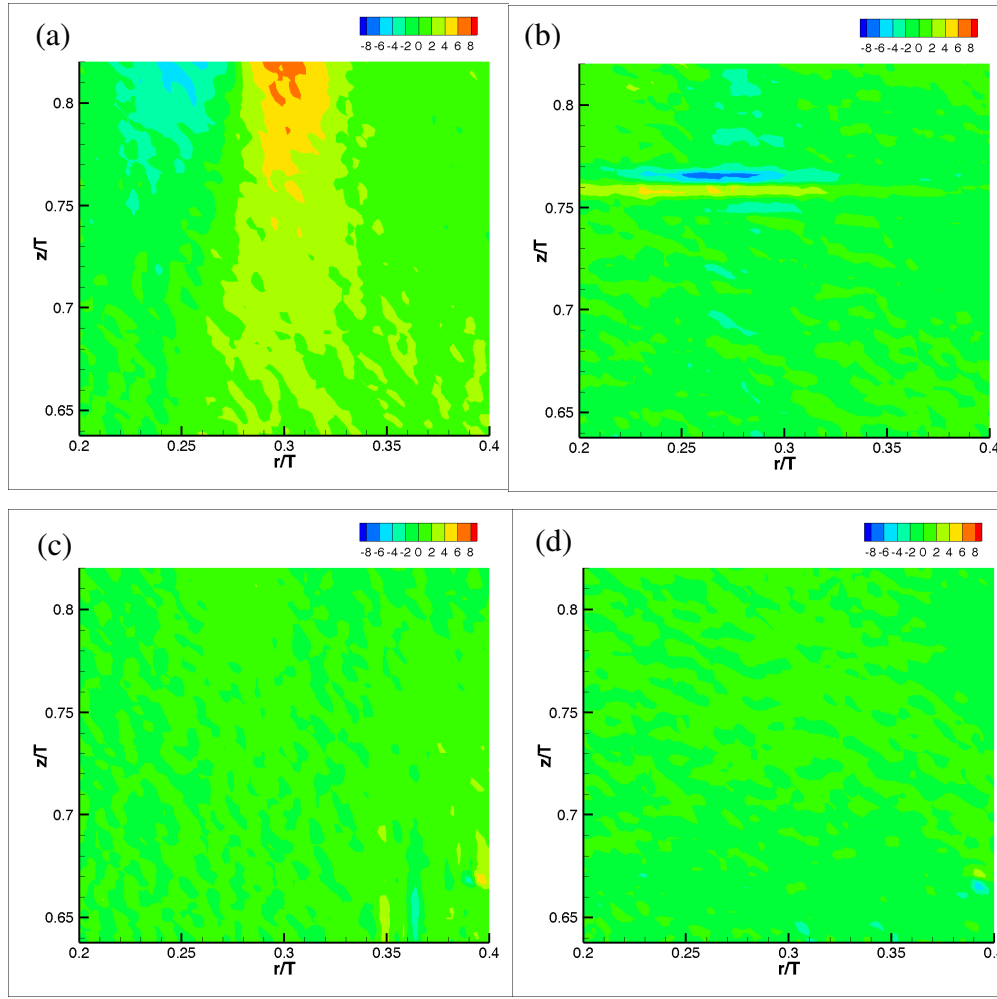


Fig. 10. Colour map of the derivative of the velocity. (a) $\frac{\partial U}{\partial r}$; (b) $\frac{\partial U}{\partial z}$; (c) $\frac{\partial V}{\partial r}$; (d) $\frac{\partial V}{\partial z}$, $N=100$ rpm. Colour scale [s^{-1}].

As can be observed, the radial gradient of the axial velocity shown in Fig. 9(a) and Fig. 10 (a) is dominant particularly close to the inlet region, while comparatively much smaller values are obtained in the rest of the domain and for the other measured components. In particular, the axial gradient of the radial velocity is much smaller, as can be observed in Fig. 9(d) and 10(d), therefore it was neglected in the turbulent viscosity calculation. The high gradients observed in Fig. 9(b) and 10(b) around $z/T=0.76$ for a limited range of radial positions are most likely due to optical disturbances in that specific locations. Different Reynolds stress components might have been more significant in other vessel regions, e.g. in the impeller discharge stream.

Similarly, the prevailing mean concentration gradient is in the radial direction, as can be observed comparing the axial and the radial gradient of the tracer concentration shown in Fig. 11, and for this reason the Γ_{11} of the diffusivity tensor was not calculated. It is worth observing

that since the mean concentration gradient is almost nil in the axial direction, while the scalar flux vectors shown in Fig. 8 are almost vertical, they are definitely not aligned and the simple gradient diffusion hypothesis cannot catch faithfully the scalar transport mechanics, similarly to the case of turbulent rectangular jet (Feng et al. 2007).

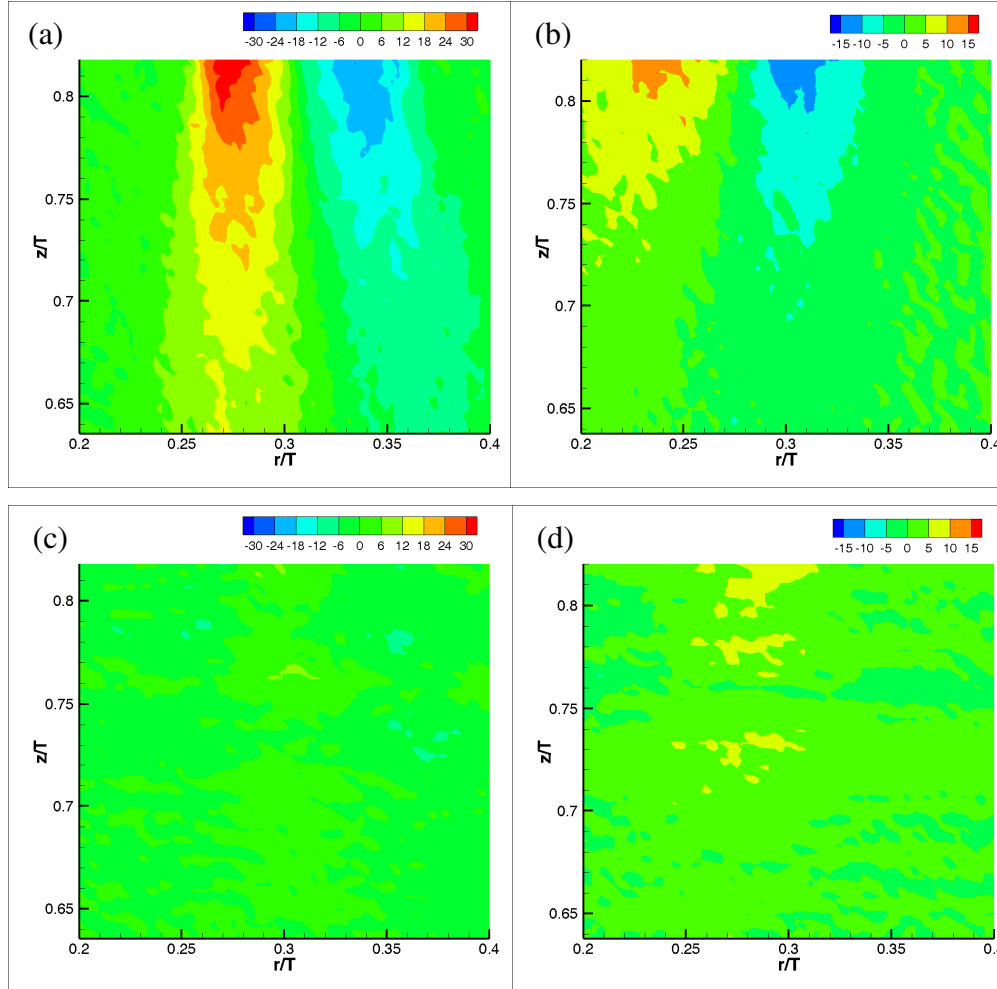


Fig. 11. Colour map of the derivative of the normalized tracer concentration. (a), (b): radial derivative; (c), (d) axial derivative. (a), (c): $N=0$ rpm; (b), (d) $N=100$ rpm. Colour scale [m^{-1}].

The turbulent viscosity shown in Fig. 12 is mainly constant in the jet region and its value is two order of magnitude bigger than the fluid kinematic viscosity, with limited variations in the plane, particularly in the case of $N=0$ rpm that is shown in Fig. 12 (a). A nil value is obtained as expected where the Reynolds stress is very small. It is also worth observing that the sign of the Reynolds stress and the mean velocity gradient are both antisymmetric with respect to the jet centreline but with opposite sign, resulting in a positive value of the turbulent viscosity, consistently with the model.

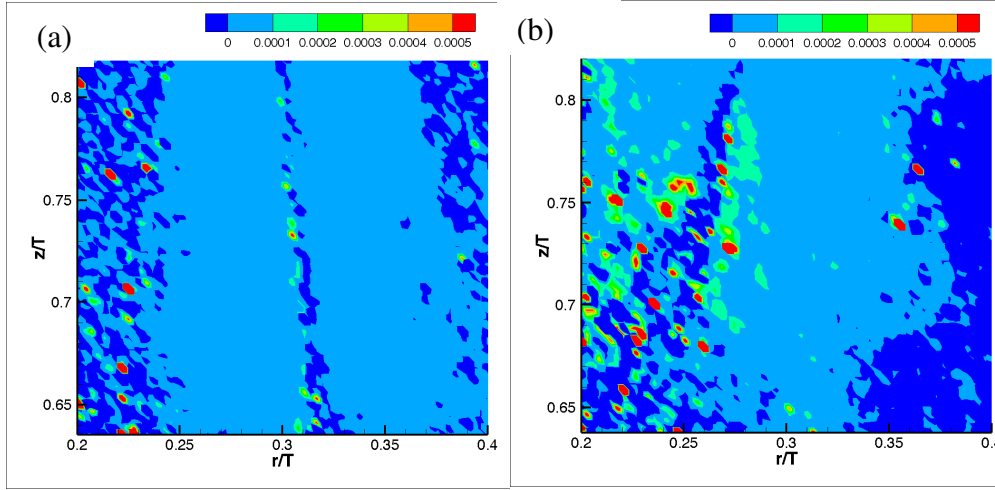


Fig. 12. Colour map of the turbulent viscosity $\nu_t = -\frac{\overline{u'v'}}{\frac{\partial U}{\partial r}}$. (a) N=0 rpm (b) N=100 rpm. Colour scale [$\text{m}^2 \text{s}^{-1}$].

The two components of the turbulent diffusivity tensor, Γ_{12} and Γ_{22} , shown in Fig. 13 and Fig. 14 both with and without agitation have similar magnitude. The antisymmetric trend of the radial mean concentration gradient is maintained from the Γ_{12} component shown in Fig. 13, while the effect is cancelled out for the turbulent diffusivity Γ_{22} , that is always positive as expected, as can be observed in Fig. 14. The non zero value of Γ_{12} confirms that also in the investigated system the adoption of a model based on a turbulent diffusivity tensor instead of a single scalar value of the turbulent diffusivity, as in the gradient diffusion hypothesis, would be probably lead to improved predictions.

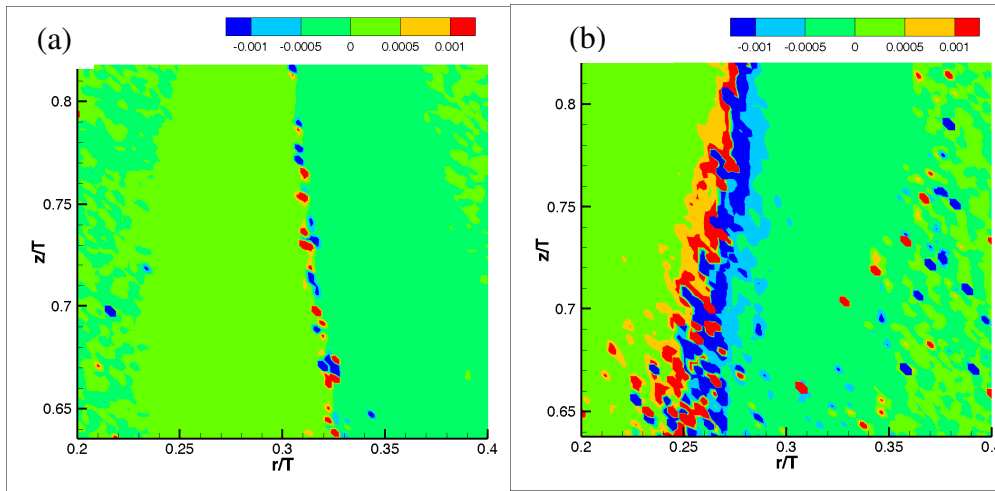


Fig. 13. Colour map of $\Gamma_{12} = -\frac{\overline{u'\phi'}}{\frac{\partial \phi}{\partial r}}$. (a) N=0 rpm (b) N=100 rpm. Colour scale [$\text{m}^2 \text{s}^{-1}$].

Local discontinuities of the turbulent diffusivity maps can be ignored, since they are due to the negligible values of the mean concentration gradient, which produce high noise in the calculated ratio.

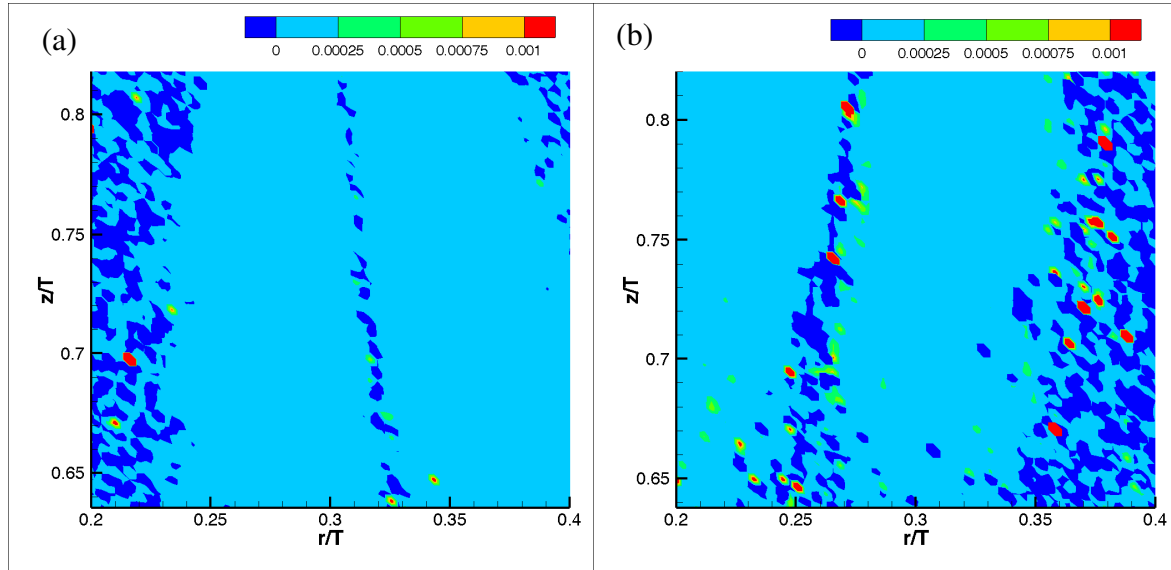


Fig. 14. Colour map of $\Gamma_{22} = -\frac{\overline{v'\phi'}}{\frac{\partial\phi}{\partial r}}$. (a) N=0 rpm (b) N=100 rpm. Colour scale [$\text{m}^2 \text{s}^{-1}$].

Finally, the map of the turbulent Schmidt number, that is calculated as the ratio between Eq. (3) and Eq. (4) and is shown in Figure 15, is mainly equal to 1 in most of the inlet region. Inside it, the discontinuities are due to the experimental approximations mentioned already and concerning the noise mainly due to the divisions by very small or nil values. Limited to the region at $0.27 < r/T < 0.34$ and $0.7 < z/T < 0.82$, based the square root of the sum of squares of the maximum error of each term contributing to the Sc calculation, an uncertainty equal to 0.25 is found. In the same region, discarding the nil values, the mean value and the variance of the turbulent Schmidt number were equal 0.71 and 1.73 respectively.

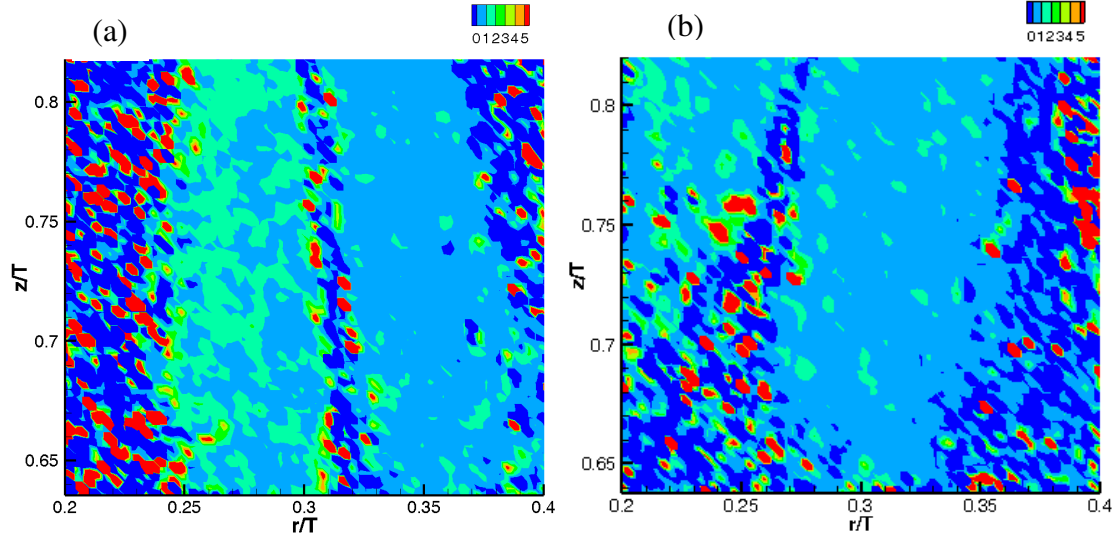
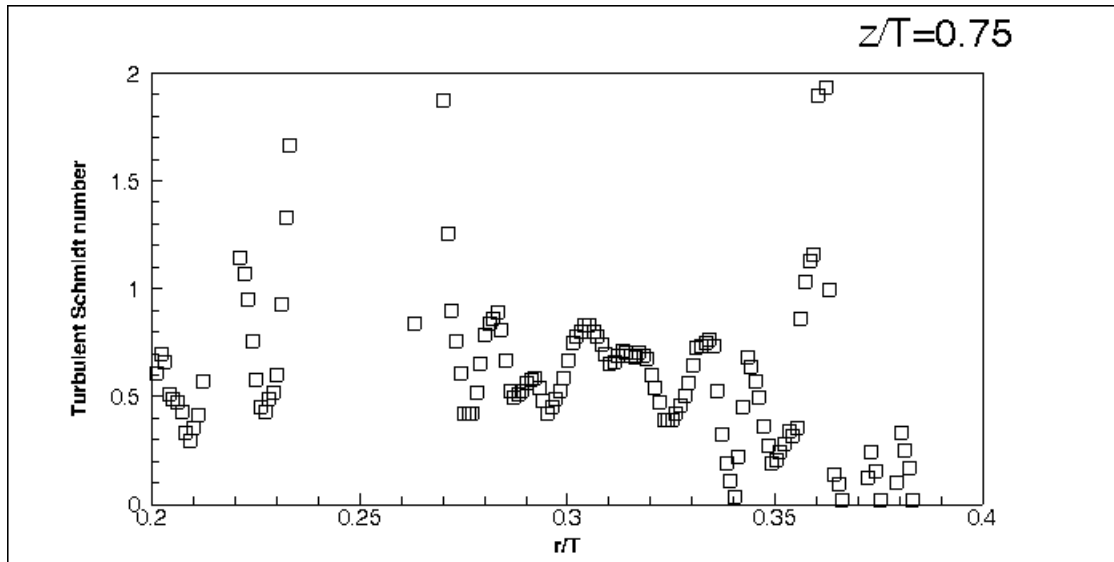


Fig. 15. Colour map of $Sc_t = \frac{\frac{u'v'}{\partial U}}{\frac{v'\phi'}{\partial r}}$ (a) N=0 rpm (b) N=100 rpm.

In order to closer observe the local value of Sc_t , the profiles along two horizontal lines located at $z/T=0.75$ and $z/T=0.80$ are shown in Fig. 16. Although the spatial variations are not negligible and it was already shown that the gradient diffusion hypothesis is a rough approximation, most of the data falls in the range 0.7-1.0, consistently with the values usually adopted for predicting the scalar transport in turbulent stirred tanks.



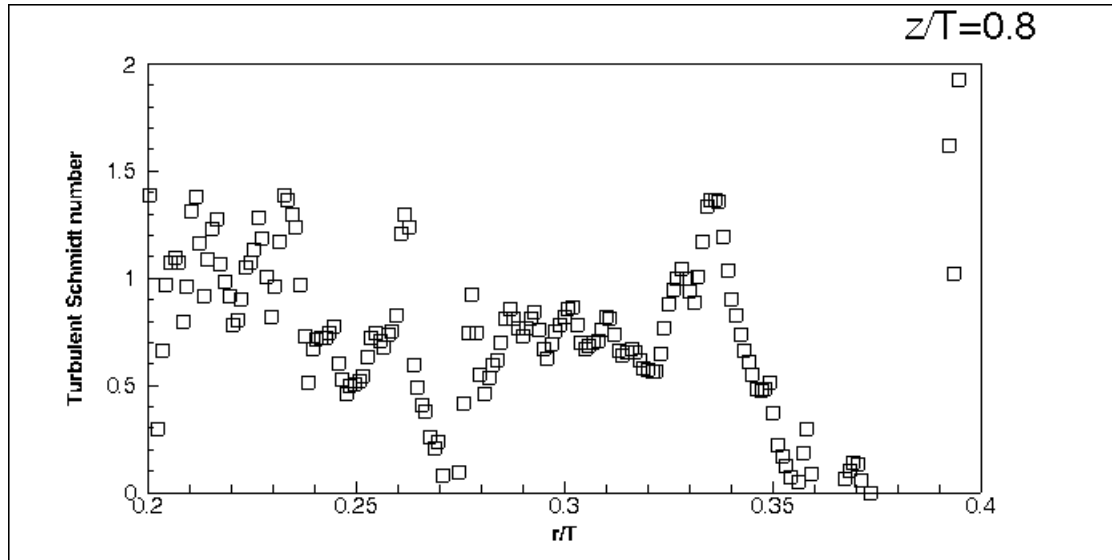


Fig. 16. Radial profiles of Sc_t at two elevations in the stirred tank ($N=100$ rpm).

4. Conclusions

In this work a combined PIV and PLIF technique has been applied for the first time to the investigation of scalar transport in stirred tanks. A detailed description of the technique is presented and the fundamental parameters to obtain reliable simultaneous velocity and concentration data are provided, with the aim of encouraging further applications of the technique and the collection of a significant amount of data, that would help in formulating more refined model equations for the turbulent transport of passive scalars in stirred tanks.

Limited to a single impeller speed in the lower limit of the turbulent flow regime, the results collected in this work show that the values of the turbulent Schmidt number usually adopted in RANS based gradient diffusion hypothesis are in the range of the experimental determinations. Nevertheless, the gradient diffusion hypothesis relying on a single scalar value of the turbulent diffusivity does not strictly apply to the investigated system, since the Reynolds flux and the tracer concentration gradient are not aligned, therefore the turbulent scalar transport predictions in stirred tanks would take advantage from the development of more refined closure models.

Acknowledgment

A. Paglianti acknowledges the support of the Italian Government through the Grant "Excellent Departments" 2018-2023.

References

- Baldi, S., Yianneskis, M. On the Direct Measurement of Turbulence Energy Dissipation in Stirred Vessels with PIV (**2003**) *Industrial and Engineering Chemistry Research*, 42 (26), pp. 7006-7016.
- Baldi, S., Ducci, A., Yianneskis, M. Determination of dissipation rate in stirred vessels through direct measurement of fluctuating velocity gradients (**2004**) *Chemical Engineering and Technology*, 27 (3), pp. 275-281.
- Busciglio, A., Montante, G., Paglianti, A. Flow field and homogenization time assessment in continuously-fed stirred tanks (**2015**) *Chemical Engineering Research and Design*, 102, pp. 42-56.
- Combest, D.P., Ramachandran, P.A., Dudukovic, M.P. On the gradient diffusion hypothesis and passive scalar transport in turbulent flows (**2011**) *Industrial and Engineering Chemistry Research*, 50 (15), pp. 8817-8823.
- Coroneo, M., Montante, G., Paglianti, A., Magelli, F. CFD prediction of fluid flow and mixing in stirred tanks: Numerical issues about the RANS simulations (**2011**) *Computers and Chemical Engineering*, 35 (10), pp. 1959-1968.
- Delafosse, A., Collignon, M.-L., Calvo, S., Delvigne, F., Crine, M., Thonart, P., Toye, D. CFD-based compartment model for description of mixing in bioreactors (**2014**) *Chemical Engineering Science*, 106, pp. 76-85.
- Doulgerakis, Z., Yianneskis, M., Ducci, A. On the interaction of trailing and macro-instability vortices in a stirred vessel-enhanced energy levels and improved mixing potential (**2009**) *Chemical Engineering Research and Design*, 87 (4), pp. 412-420.
- Escudié, R., Liné, A. Experimental analysis of hydrodynamics in a radially agitated tank (**2003**) *AIChE Journal*, 49 (3), pp. 585-603.
- Feng, H., Olsen, M.G., Liu, Y., Fox, R.O., Hill, J.C. Investigation of turbulent mixing in a confined planar-jet reactor (**2005**) *AIChE Journal*, 51 (10), pp. 2649-2664.
- Feng, H., Olsen, M.G., Hill, J.C., Fox, R.O. Simultaneous velocity and concentration field measurements of passive-scalar mixing in a confined rectangular jet (**2007**) *Experiments in Fluids*, 42 (6), pp. 847-862.
- Feng, H., Olsen, M.G., Hill, J.C., Fox, R.O. Investigation of passive scalar mixing in a confined rectangular wake using simultaneous PIV and PLIF (**2010**) *Chemical Engineering Science*, 65 (11), pp. 3372-3383.
- Gualtieri, C., Angeloudis, A., Bombardelli, F., Jha, S., Stoesser, T. On the values for the turbulent schmidt number in environmental flows (**2017**) *Fluids*, 2 (2), art. no. 17.

- Haringa, C., Vandewijer, R., Mudde, R.F. Inter-compartment interaction in multi-impeller mixing: Part I. Experiments and multiple reference frame CFD **(2018)** *Chemical Engineering Research and Design*, 136, pp. 870-885.
- Hartmann, H., Derksen, J.J., Van Den Akker, H.E.A., Mixing times in a turbulent stirred tank by means of LES **(2006)** *AIChE Journal*, 52 (11), pp. 3696-3706.
- Hitimana, E., Fox, R.O., Hill, J.C., Olsen, M.G. Experimental characterization of turbulent mixing performance using simultaneous stereoscopic particle image velocimetry and planar laser-induced fluorescence **(2019)** *Experiments in Fluids*, 60 (2), art. no. 28.
- Houcine, I., Vivier, H., Plasari, E., David, R., Villiermaux, J. Planar laser induced fluorescence technique for measurements of concentration fields in continuous stirred tank reactors **(1996)** *Experiments in Fluids*, 22 (2), pp. 95-102.
- Li, G., Li, Z., Gao, Z., Wang, J., Bao, Y., Derksen, J.J. Particle image velocimetry experiments and direct numerical simulations of solids suspension in transitional stirred tank flow **(2018)** *Chemical Engineering Science*, 191, pp. 288-299.
- Liu M. Age distribution and the degree of mixing in continuous flow stirred tank reactors **(2012)** *Chemical Engineering Science*, 69, 382-393.
- Liu, Y., Feng, H., Olsen, M.G., Fox, R.O., Hill, J.C. Turbulent mixing in a confined rectangular wake **(2006)** *Chemical Engineering Science*, 61 (21), pp. 6946-6962.
- Montante, G., Paglianti, A., Magelli, F. Analysis of dilute solid-liquid suspensions in turbulent stirred tanks **(2012)** *Chemical Engineering Research and Design*, 90 (10), pp. 1448-1456.
- Papadopoulos G. and Arik E. B. Experimental Methods. Part B: Fundamental Flow Measurement Chapter 4 in: Handbook of Industrial Mixing, Paul, E.L., Otiemo-Obeng, V.A. and Kresta, S.M. (eds), (Wiley-Interscience, Hoboken, N.J., USA), pp. 202-203, **2004**.
- Stamatopoulos, K., Alberini, F., Batchelor, H., Simmons, M.J.H. Use of PLIF to assess the mixing performance of small volume USP 2 apparatus in shear thinning media **(2016)** *Chemical Engineering Science*, 145, pp. 1-9.
- Su, L.K., Mungal, M.G. Simultaneous measurements of scalar and velocity field evolution in turbulent crossflowing jets **(2004)** *Journal of Fluid Mechanics*, 513, pp. 1-45.
- Yianneskis, M., Whitelaw, J.H. On the structure of the trailing vortices around Rushton turbine blades **(1993)** *Chemical Engineering Research and Design*, 71 (A5), pp. 543-550.